

Practical approaches to study microbially induced calcite precipitation at the field scale

D. Landa-Marbán¹ S. Tveit¹ K. Kumar² S.E. Gasda¹

¹ NORCE Norwegian Research Centre AS, Nygårdsgaten 112, 5008 Bergen, Norway.

² Department of Mathematics, Faculty of Mathematics and Natural Sciences, University of Bergen, Allégaten 41, 5020 Bergen, Norway.

Corresponding author: David Landa-Marbán (E-mail address: dmar@norceresearch.no).

Abstract

Microbially induced calcite precipitation (MICP) is a new and sustainable technology which utilizes biochemical processes to create barriers by calcium carbonate cementation; therefore, this technology has a potential to be used for sealing leakage zones in geological formations. The complexity of current MICP models and present computer power limit the size of numerical simulations. We describe a mathematical model for MICP suitable for field-scale studies. The model is simple enough to have a few equations but still retain the essence of the processes. The main mechanisms in the conceptual model are as follow: microbes attach themselves to the pore walls to form biofilm, the biofilm consumes substrate to grow, the biofilm use urea for production of calcite, and the calcite reduce the pore space which in turn decreases the rock permeability. We apply the model to study the MICP technology in two sets of reservoir properties including a well-established field-scale benchmark system for CO₂ leakage. A two-phase flow model for CO₂ and water is used to assess the leakage prior to and with MICP treatment. Based on the numerical results, this study confirms the potential for this technology to seal leakage paths in reservoir-caprock systems.

Keywords Carbon capture and storage (CCS) · Leakage mitigation and remediation · Mathematical modelling · Microbially induced calcite precipitation (MICP) · Reactive transport

1 Introduction

Negative emissions technologies and carbon storage must be implemented to avoid dangerous climate changes (Haszeldine et al., 2018; Tong et al., 2019). Carbon capture and storage (CCS) is one of the promising scalable technologies for storing large amounts of CO₂. Indeed, large amounts of CO₂ have already been stored in geological formations on the Norwegian continental shelf, e.g., in the Sleipner field, where more than 16 Mt CO₂ has been stored since 1996 (Furre et al., 2017). Caprocks in reservoirs provide the main trapping mechanism for CO₂ sequestration (Bentham and Kirby, 2005). The existence of faults, fractures, and abandoned wells in the primary sealing caprock of a CO₂ storage reservoir can create pathways for CO₂ to migrate back to the surface (Fang et al., 2010). Fig. 1 shows a schematic representation of CO₂ sequestration, where fractures in the caprock are a risk to leak CO₂ back to the atmosphere and to fresh water.

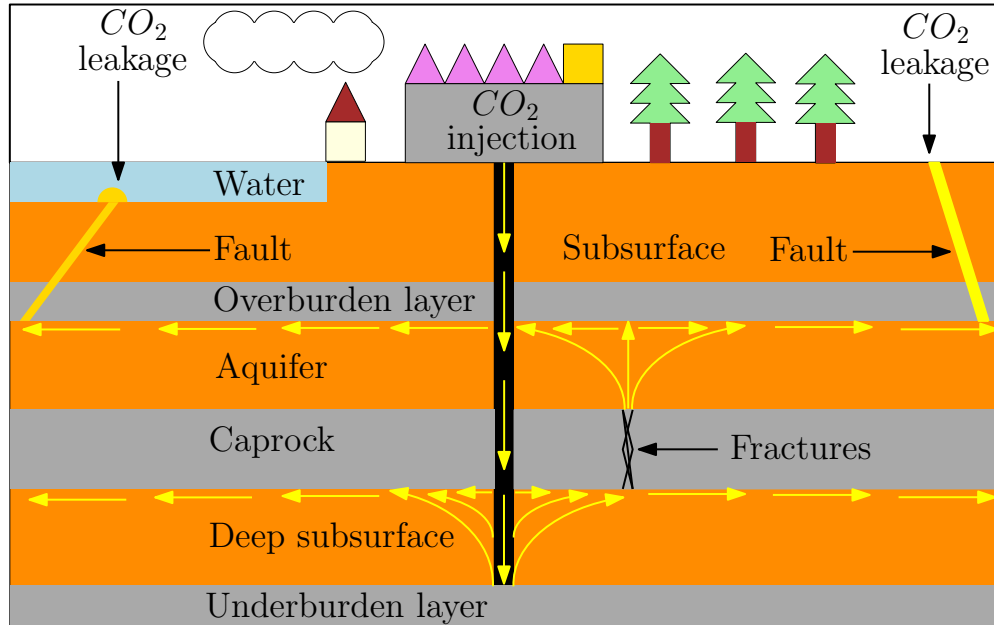


Figure 1: Contamination of water and atmosphere by CO₂ leakage.

It is therefore necessary to develop methods for mitigating CO₂ leakage to ensure its long-term storability. One of the proposed remediation measures to seal leakage zones is the use of microbes to induce precipitation of calcium carbonate (Phillips et al., 2016). Microbially induced calcite precipitation (MICP) is a new and sustainable technology which utilizes biochemical processes to create barriers by calcium carbonate cementation. The MICP technology involves the injection of diverse components into a reservoir such as microbes, substrate, and chemicals. As calcite permeability is very low, then the formation of calcite decreases the rock permeability. Thus, MICP technology has a potential to be used for sealing leakage zones in geological formations. These barriers can significantly reduce CO₂ leakage even when the leakage channels are not fully plugged (Li et al., 2019). Among other applications of MICP besides as a leakage prevention tool in CO₂ sequestration are in biomineralized concrete (Lee et al., 2018), improvement in the stiffness and strength of granular soils (Jalili et al., 2018; Whiffin et al., 2007), wastewater treatment (Torres-Aravena et al., 2018), and erosion control (Jiang and Soga, 2017).

MICP as a leakage mitigation technology is intended for use on the field scale, but performing field-scale experiments is expensive. Experiments on microsystems allow us to observe processes in more detail, which leads to improvements in core-scale experiments prior to field applications. We mention some notable works in this direction. Bai et al. (2017) performed MICP experiments in microfluidic cells to study the distribution of calcite precipitation at the pore scale and observed that calcite precipitation occurs mainly on the bottom of biofilms. Core samples from reservoirs can be used to study changes in permeability due to biofilm growth and calcite precipitation. For example, Whiffin et al. (2007) conducted a core-scale experiment to evaluate MICP as a soil strengthening process. Since the laboratory experiment was conducted under field conditions and a significant improvement of strength was observed along the column, the authors concluded that MICP can be used for large-scale applications. Ebigbo et al. (2012) performed core-scale experiments under controlled conditions for studying the effect of calcite precipitation in porous media. The authors tested different injection strategies to obtain a homogeneous distribution of calcite precipitation along sand-packed columns. Their work provides a successful injection strategy for this purpose and experimental data of four columns. Mitchell et al. (2013) investigated the MICP processes in a core sample inside a high pressure flow reactor including supercritical CO₂ to simulate field

conditions. Their experimental results show that MICP can be applied in the presence of supercritical CO₂. [Gomez et al. \(2017\)](#) performed experiments in tanks of 1.7 m diameter and with three wells to study the reactive transport of MICP. Their results show that indigenous microorganisms could be stimulated for MICP in field-scale applications. Based on these and more experimental work reported in literature, mathematical models of this technology can be built for further studies.

Mathematical models of MICP are important as they help to predict the applicability of this technology and to optimize its benefits. [Zhang and Klapper \(2010\)](#) introduced a comprehensive pore-scale model for MICP which includes chemistry, mechanics, thermodynamics, fluid, and electrodiffusion transport effects. The authors performed simulations under different conditions of flow rates, concluding that the flow significantly impact the calcite distribution. [Hommel et al. \(2015\)](#) introduced a core-scale mathematical model for MICP which includes chemistry, mechanics, and fluid transport effects. The authors also calibrated some of the model parameters with experimental data. [Minto et al. \(2019\)](#) proposed a mathematical model for MICP and performed numerical studies of calcite precipitation around a production well using eight surrounding injection wells. The authors concluded that uniform calcite precipitation could be achieved by splitting the injection into phases, where different number of wells are used in each of the injection phases. Note that “phases” is used to denote both physical phases and repeatable steps in the injections strategies, and the meaning will be clear from the context.

Despite advances in modeling, simulation of the MICP process at the field-scale is challenging as current mathematical models involve the solution of large systems of highly coupled partial differential equations. In [Cunningham et al. \(2019\)](#) the authors suggest different approaches to handle this issue such as refinement of the grid locally, multi-scale methods, improving the time stepping, or reducing the coupling of the model equations. [Tveit et al. \(2018\)](#) proposed a simplified version of the MICP model presented in [Hommel et al. \(2015\)](#) to perform field-scale simulations. The authors study two different approaches for inducing calcite precipitation at a given distance of an injection well. Since the complexity of current MICP models and present computer power limit the size of numerical simulations, then simplified models are needed to perform field-scale studies. In this work, we build a single-phase field-scale model of MICP technology. This model includes the transport of dissolved components (microbes, substrate, and urea), biofilm activity (microbial attachment, death, detachment, and growth), and production of calcite which reduce the rock porosity and hence the effective permeability. We use the model to investigate the prevention and sealing of leakage paths located at a certain distance away from the injection well. A simple two-phase flow model for CO₂ and water is used to assess the leakage prior to and with MICP treatment.

Our motivation to develop the mathematical model and numerical tools is as follows. We aim to have a model that captures the key processes and quantities involved in the MICP process. At the same time, we aim to have a model which is simple enough so that computational costs are less. Our main reason for the latter is that the field-scale processes require running the model on a large scale and also require multiple simulations to perform optimization studies. All these imply a heavy computational burden unless we simplify the model. Needless to say, the simplified model should still retain the essence of the processes so that it is useful. Our work is therefore a step in this direction of achieving the twin objectives.

The paper is structured as follows. In Section 2 we explain in detail the MICP mathematical model, the model parameters, the computer implementation of the model, and the injection strategy. Diverse field-scale numerical experiments to prevent CO₂ leakage using MICP are presented in Section 3. A discussion on the numerical results and findings is given in Section 4. Finally, we present the conclusions in Section 5.

2 MICP model

In this section we describe the mathematical model for MICP, introducing first concepts and definitions related to this technology. Fig. 2 shows a schematic representation of the sealing mechanism using MICP. Here, we observe a fractured zone in the caprock being remediated by calcite.

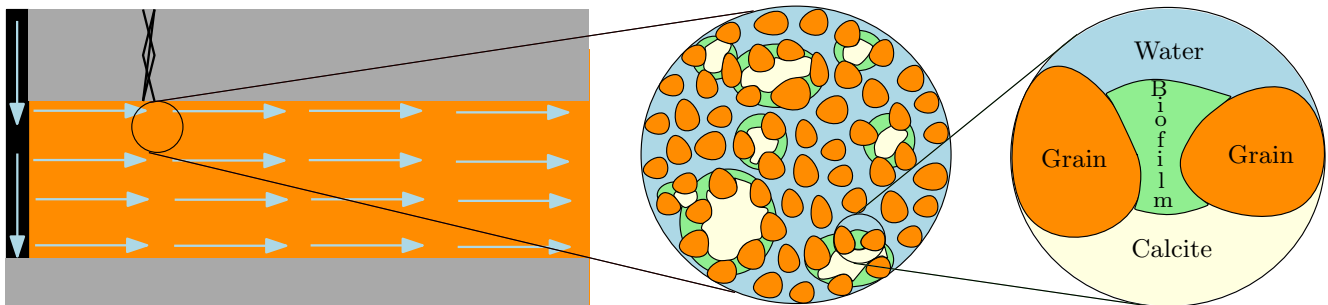


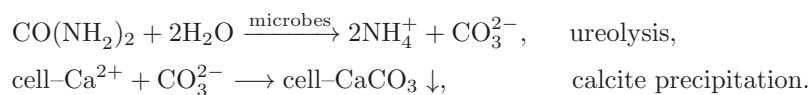
Figure 2: Sealing leakage paths with calcite using MICP.

MICP can be defined as a bio-geochemical process which results in precipitation of calcite (the low-pressure, hexagonal form of CaCO_3). Calcium carbonate (CaCO_3) is a mineral that naturally precipitate as a result of microbial metabolic activities. Biofilm formation is a process whereby microorganisms attach themselves to a surface and produce an adhesive matrix of extracellular polymeric substances (EPS). A biofilm requires different factors for survival, e.g., nutrients and oxygen (for aerobic microbes). In this work, we denote the solution which includes all the different components a biofilm needs for growing (e.g., nutrients, oxygen) as substrate. In addition, we denote suspended biomass in water as microbes. Urea [$\text{CO}(\text{NH}_2)_2$] is a water-soluble compound found in the urine and other bodily fluids of mammals or produced synthetically. Urease is an enzyme catalyzing the hydrolysis of urea to ammonium (NH_4^+) and carbonate (CO_3^{2-}). *Sporosarcina pasteurii* is a non-pathogenic bacterium commonly used for the MICP process as it shows a high urease enzyme activity (Bhaduri et al., 2016). Calcium (Ca^{2+}) is a mineral which contributes to processes of organisms cell. With the main concepts introduced, we proceed to describe the conceptual and mathematical model of MICP used in this paper.

2.1 Conceptual model

We consider a constant-temperature reservoir saturated with water, where calcite and biofilm only occur on the rock walls, i.e., in the space domain there are one liquid phase (water) and three solid phases (biofilm, calcite, and rock matrix). The microbes, substrate, and urea are dissolved in water prior to injection and they are transported only in the water phase by advection and dispersion. The biofilm and calcite are assumed to be impermeable and incompressible. The governing processes in the biofilm are growth, death, attachment, and detachment.

The most studied MICP process is urea hydrolysis (ureolysis) via the enzyme urease produced by special microbes, in a calcium-rich environment (Rong et al., 2012; Whiffin et al., 2007):



In general, CaCO_3 precipitation is governed by four main factors (Hammes and Verstraete, 2002): calcium concentration, carbonate concentration, pH, and availability of nucleation sites. Lauchnor et al. (2015) performed experiments on *S. pasteurii*, showing that urea and microbial concentration have a more significant impact on the

ureolysis rate than pH variations. In addition, we consider that the amount of urease is only related to the amount of biofilm, neglecting the microbes in the liquid phase as its contribution is minor (Ebigbo et al., 2012). Assuming enough calcium concentration in the water, we model the calcite formation as a function only dependent on urea and biofilm. This assumption can be justified since calcium and urea can be injected together, and would thus distribute in a similar manner, ensuring that both concentrations are high in the location where calcite precipitation is aimed.

To summarize, the system of interest consists of a 3D reservoir (porous medium), one source (injection well), one fluid phase (water), two solid phases (biofilm and calcite), and three transported components (microbes, substrate, and urea).

2.2 Mathematical model

We build a mathematical model based on the assumptions laid out in the conceptual model. We adopt a continuum approach, where the processes in the system are described by conservation laws and coupling relationships. We use the subscripts $\{b, c, m, s, u, w\}$ to refer to biofilm, calcite, microbes, substrate, urea, and water respectively.

2.2.1 Flow equations

The mass conservation and Darcy’s law equations for the water phase are given by:

$$\frac{\partial \phi}{\partial t} + \nabla \cdot \mathbf{v}_w = q_w, \quad \mathbf{v}_w = -\frac{\mathbb{K}}{\mu_w} (\nabla p_w - \rho_w \mathbf{g}) \quad (1)$$

where ϕ is the rock porosity, p_w the reservoir pressure, \mathbf{v}_w the flow velocity, ρ_w the fluid density, \mathbb{K} the absolute permeability, \mathbf{g} the gravity, μ_w the water viscosity, and q_w the source/sink term.

2.2.2 Leakage paths

We adopt a common approach found in Class et al. (2009), where the leakage paths in the caprock are modeled as a porous medium with higher permeability than the formation. An advantage of this approach is that the model equations do not need further modification for implementation while a drawback is that it requires a fine grid to represent explicitly the leakage paths. This may be contrasted with the widely-used approach of discrete fracture networks (DFN) where one uses a mixed dimensional setting and represents the fractures as a $n - 1$ dimensional objects embedded in a n dimensional porous geometry. We refer to Berre et al. (2019) for a recent review of different conceptual models for fracture and Kumar et al. (2020) and Martin et al. (2005) for a formal derivation of some of these models. We also mention that our model here can be easily adapted for different conceptual models including fractures being modeled as DFNs.

2.2.3 Injection well

In this work we consider only one injection well, where we use the following linear law to relate the injection rate Q_w (Lie, 2019; Peaceman, 1978):

$$Q_w = \frac{2\pi h K}{\mu_w \ln(r_e/r_I)} [p_I - p_w - \rho_w(z - z_{bh})g]. \quad (2)$$

Here, p_I is the pressure inside the wellbore, h is the height of the well, r_I the well radius, z_{bh} a reference depth (perforation), K is the permeability in the direction of the injection, and r_e an equivalent radius at which the cell

pressure is equal to the average of the exact pressure.

2.2.4 Transport equations

To describe the transport of microbes, substrate, and urea, we consider the following advection-dispersion-reaction transport equations:

$$\frac{\partial(c_\xi\phi)}{\partial t} + \nabla \cdot \mathbf{J}_\xi = c_\xi q_w + R_\xi, \quad \mathbf{J}_\xi = -\phi \mathbb{D}_\xi \nabla c_\xi + c_\xi \mathbf{v}_w, \quad \xi \in \{m, s, u\}. \quad (3)$$

Here, c_ξ is the concentration of component ξ in water, \mathbf{J}_ξ the flux of ξ , R_ξ the reaction term of ξ , and \mathbb{D}_ξ the dispersion tensor. Here, we assume that the aqueous phase density does not depend on the component concentrations.

2.2.5 Dispersion effects

When the components are transported throughout the reservoir, two different mechanisms affect their movement: mechanical dispersion and molecular diffusion. The former is an effect arising out of mixing due to flow and heterogeneities while the latter accounts for movement of the components from a region of higher to lower concentration. We adopt the following model for the dispersion of components (Bear, 1972)

$$\mathbb{D}_\xi = \alpha_T \|\mathbf{v}\| \mathbb{I} + (\alpha_L - \alpha_T) \frac{\mathbf{v} \otimes \mathbf{v}}{\|\mathbf{v}\|} + D_\xi \mathbb{I}, \quad \xi \in \{m, s, u\}, \quad (4)$$

where α_L and α_T are the longitudinal and transverse dispersion coefficients, $\mathbf{v} = \mathbf{v}_w/\phi$ is the effective velocity of the aqueous phase, and D_ξ the effective diffusion coefficient of component ξ .

2.2.6 Solid-phase equations

As previously mentioned, we consider biofilm formation and calcite precipitation fixed in space (at the pore scale, it represents the biofilm and calcite precipitate at the rock surface). Thus, the following mass balance equations describe the evolution of biofilm and precipitation of calcite

$$\frac{\partial(\rho_\chi \phi_\chi)}{\partial t} = R_\chi, \quad \chi \in \{b, c\}, \quad (5)$$

where ρ_χ are densities and R_χ accounts for the calcite and biofilm processes and are being described later in this section.

2.2.7 Substrate consumption

The substrate consumption rate R_s is modeled by the Monod equation

$$R_s = -(c_m \phi + \rho_b \phi_b) \mu_s \frac{c_s}{k_s + c_s} \quad (6)$$

where μ_s is the maximum rate of substrate utilization and k_s is the half-velocity coefficient for the substrate.

2.2.8 Urea utilization

The urea conversion rate R_u is modeled by the Monod equation (Hommel et al., 2015; Lauchnor et al., 2015)

$$R_u = -\rho_b \phi_b \mu_u \frac{c_u}{k_u + c_u}, \quad (7)$$

where μ_u is the maximum rate of urea utilization and k_u is the half-velocity coefficient for urea. This model for ureolysis was introduced in Hommel et al. (2015) based on the work by Lauchnor et al. (2015), where μ_u is split into maximum urease activity and mass ratio of urease to biofilm.

2.2.9 Calcite precipitation

The calcite precipitation is the result of a complex geochemical process. Qin et al. (2016) stated that in a calcium-rich environment, when only the final calcite distribution is of interest, an approximation of the calcite precipitation rate can be given by the negative value of the urea utilization rate (i.e., $R_c = -R_u$). Since the molar mass of urea is different from calcite, we add a yield coefficient Y_{uc} (units of produced calcite over units of urea utilization) to account for this in the mathematical model. Then, we write the calcite production rate as

$$R_c = \rho_b \phi_b Y_{uc} \mu_u \frac{c_u}{k_u + c_u}. \quad (8)$$

We note that R_c only depends on the amount of biofilm and urea, which significantly reduces the computational cost compared to more complex formulations [e.g., Ebigbo et al. (2012), Hommel et al. (2015), and Minto et al. (2019)].

2.2.10 Microbes

Two opposing processes determine the evolution of microbes: growth and loss. The growth term comprises of two contributions. First, the consumption of substrate by the microbes lead to its growth. This is modeled by a Monod equation $c_m \phi Y_{sb} \mu_s c_s / (k_s + c_s)$ where Y_{sb} is a yield coefficient (units of produced biomass over units of consumed substrate). Second, its growth taking place via detachment or erosion of biofilm due to flow. Microbes detach from the biofilm back to the water phase due to shear forces on the interface by the water flow. The erosion is modeled by $\phi_b \rho_b k_{str} \phi \|\nabla p_w - \rho_w \mathbf{g}\|^{0.58}$ where k_{str} is the detachment rate (Rittmann, 1982). The loss term also has two contributions. First, the death of the microbes as a result of aging, which is modeled by a linear death rate $-c_m \phi k_d$ where k_d is the microbial death coefficient. Second, the microbes attach themselves to the pore wall and biofilm. This is modeled by a linear attachment rate $-c_m \phi k_a$ where k_a is the microbial attachment coefficient. In sum, the rate for the microbes R_m is given by

$$R_m = c_m \phi \left(Y_{sb} \mu_s \frac{c_s}{k_s + c_s} - k_d - k_a \right) + \phi_b \rho_b k_{str} \phi \|\nabla p_w - \rho_w \mathbf{g}\|^{0.58}. \quad (9)$$

2.2.11 Biofilm processes

As in the case of microbes above, the biofilm development is determined by the net of its growth and loss. Consumption of substrate by the biofilm lead to its growth. This is modeled by the Monod equation $\rho_b \phi_b Y_{sb} \mu_s c_s / (k_s + c_s)$. The microbes in the biofilm die as a result of aging and being encapsulated by the produced calcite (De Muynck et al., 2010). The former is modeled by a linear death rate $-\rho_b \phi_b k_d$ while the latter by $-\rho_b \phi_b R_c / [\rho_c (\phi_0 - \phi_c)]$ (Ebigbo et al.,

2012). As described previously, the microbial attachment leading to its growth is modeled by $c_m \phi k_a$ while the erosion leading to its loss is expressed by $-\phi_b \rho_b k_{str} \phi \|\nabla p_w - \rho_w \mathbf{g}\|^{0.58}$. In sum, the rate for the evolution of the biofilm is given by

$$R_b = \rho_b \phi_b \left[Y_{sb} \mu_s \frac{c_s}{k_s + c_s} - k_d - \frac{R_c}{\rho_c (\phi_0 - \phi_c)} - k_{str} \phi \|\nabla p_w - \rho_w \mathbf{g}\|^{0.58} \right] + c_m \phi k_a. \quad (10)$$

2.2.12 Porosity reduction

The void space in the porous medium change in time as a function of the biofilm and calcite volume fractions ϕ_b and ϕ_c respectively. Using the definitions of ϕ_b and ϕ_c , we have the following equality

$$\phi = \phi_0 - \phi_b - \phi_c. \quad (11)$$

2.2.13 Permeability modification

Porosity-permeability relationships are used frequently in mathematical modeling to account for permeability reduction as a result of biofilm and calcite growth. Diverse porosity-permeability relationships have been proposed for the last decades. These relationships can also include the permeability of biofilm and be derived as a result of upscaling pore-scale models (Landa-Marban et al., 2020; van Noorden et al., 2010). In this paper, we follow Thullner et al. (2002) and use a porosity-permeability relationship where significant reduction in CO₂ leakage can be achieved even when the leakage paths are not fully plugged,

$$\mathbb{K} = \left[\mathbb{K}_0 \left(\frac{\phi - \phi_{crit}}{\phi_0 - \phi_{crit}} \right)^\eta + K_{min} \right] \frac{\mathbb{K}_0}{\mathbb{K}_0 + K_{min}}. \quad (12)$$

Here, \mathbb{K}_0 is the initial rock permeability, ϕ_{crit} is the critical porosity when the permeability becomes a minimum value K_{min} , and η is a fitting factor.

2.2.14 Remarks on the MICP model

The development of the present mathematical model is inspired by previous works on the MICP technology (Cunningham et al., 2019; Ebigbo et al., 2012; Hommel et al., 2015; Lauchnor et al., 2015; Qin et al., 2016). One of the most complete models for the MICP technology is presented in Hommel et al. (2015). This MICP model includes detailed chemistry reactions, mechanics, and fluid transport effects. Given the complexity of the model and the current computing power, solving simultaneously all equations would limit the size of the problem. Hence we build a simpler mathematical model so that the computational costs are less but the essence of the processes is retained. We summarize the main assumptions that we have adopted to build the simplified MICP model: only one fluid phase (water) and two solid phases (calcite and biofilm) are presented, there are only three transported components (microbes, substrate, and urea) dissolved in the fluid phase, the amount of urease is only related to the amount of biofilm, and the calcite formation only depends on urea and biofilm. The mathematical model is given by Eqs. (1-12). This model consists of six mass balance equations and six cross coupling constitutive relationships.

2.3 Implementation

The EOR module in the MATLAB[®] reservoir simulation tool (MRST), a free open-source software for reservoir modeling and simulation, is modified to implement the MICP mathematical model (Bao et al., 2017; Lie, 2019). Specifically, the polymer example (black-oil model + one transport equation) is modified (single-phase flow + three

transport equations + two mass balance equations) to solve the MICP mathematical model. A comprehensive discussion of the solution of the polymer model can be found in [Bao et al. \(2017\)](#). The MICP mathematical model is solved on domains with cell-centered grids. Two-point flux approximation (TPFA) and backward Euler (BE) are used for the space and time discretization respectively. The resulting system of equations is linearized using the Newton-Raphson method. In contrast to the polymer model, we implement dispersion of the transported components, permeability changes due to calcite and biofilm formation, and biofilm detachment due to shear forces. The spatial discretization is performed using internal functions in MRST and the external mesh generator DistMesh ([Persson and Strang, 2004](#)). The MICP processes can be simulated over time and the simulator stops when full-plugging of at least one cell is reached (i.e., $\phi = 0$). The links to download the corresponding code can be found above the references at the end of the manuscript.

2.4 Model parameters

Mathematical models require the numerical values of coefficients in the equations to be solved. These model parameters are system-dependent and their values are estimated by different means, e.g., direct measurements of the system and experimental data. Experiments under controlled input quantities aim to provide a better estimation of these parameters. For example, in [Landa-Marban et al. \(2019\)](#) the detachment rate for the bacterium *Thalassospira* strain A216101 was estimated after performing measurements of the biofilm development under different flow rates. The MICP mathematical model consists of 21 model parameters whose value may depend on the species of bacteria, temperature in the system, rock type, substrate, etc. In this work, we use model parameters reported in the literature.

Table 1 summarizes the model parameters for the numerical simulations. We comment on the maximum rate of urea utilization μ_u , yield coefficient Y_{uc} , and minimum permeability K_{\min} . [Lauchnor et al. \(2015\)](#) estimated values for the kinetics of ureolysis by *S. pasteurii*. We consider a value of $\mu_u = 1.61 \times 10^{-2} \text{ s}^{-1}$ [here we use the value of mass ratio of urease to biofilm of 3.81×10^{-4} and 0.06 kg/mol for urea multiplied by 706.7 mol/(kg s) ([Lauchnor et al., 2015](#))]. The molar mass ratio of calcite (0.1 kg/mol) to urea gives a value of 1.67 for the yield coefficient Y_{uc} . The value of K_{\min} is set to 10^{-20} m^2 which is of the order of magnitude of permeability in a caprock to retain fluids for CCS ([Schlumberger, 2020](#)).

The equivalent radius r_e for the injection well depends on the grid. For a domain with rectangular grid blocks, the equivalent radius is given by $r_e = 0.14\sqrt{\Delta x^2 + \Delta y^2}$ ([Peaceman, 1978](#)). We set the well radius to $r_1=0.15 \text{ m}$ ([Ebigbo et al., 2007](#)). Regarding input concentrations, the maximum amount of urea dissolved in water is limited by its solubility, e.g., 1079 kg/m³ at 20 °C. In the MICP experiment reported in [Whiffin et al. \(2007\)](#) the concentration of urea corresponds to 66 kg/m³. The concentration of microbes is typically given in colony forming units (CFU) or in optical density of a sample at 600 nm (OD₆₀₀). Two values of concentrations for *S. pasteurii* used in experiments and reported in literature are $4 \times 10^7 \text{ CFU/ml}$ and 1.583 OD₆₀₀. The former is equivalent to 0.01 kg/m³ using a cell weight of $2.5 \times 10^{-16} \text{ kg/CFU}$ ([Norland et al., 1987](#)) while the latter is approximately equal to $17 \times 10^8 \text{ CFU/ml}$ ([Jin et al., 2018](#)), which, using the cell weight, is converted to 0.425 kg/m³. Different substrate concentrations are reported in literature, e.g., 5 kg/m³ of cellobiose ([Linville et al., 2013](#)). Here we consider the following concentrations: $c_m=0.01 \text{ kg/m}^3$, $c_s=1 \text{ kg/m}^3$, and $c_u=66 \text{ kg/m}^3$. While the urea and microbial concentrations are taken from laboratory experiments, we choose a substrate concentration such that the substrate is totally consumed by the microbes.

Different studies can be conducted on mathematical models with a few parameters. For example, sensitivity analysis on the mathematical model allows us to identify critical model parameters. We refer to [Landa-Marban et al.](#)

Table 1: Table of model parameters for the numerical studies

Parameter	Symbol	Value	Unit	Reference
Density (biofilm)	ρ_b	35	kg/m ³	Hommel et al. (2015)
Density (calcite)	ρ_c	2710	kg/m ³	Standard
Density (water)	ρ_w	1045	kg/m ³	Ebigbo et al. (2007)
Detachment rate	k_{str}	2.6×10^{-10}	m/Pa s	Landa-Marbán et al. (2019)
Critical porosity	ϕ_{crit}	0.1	[-]	Hommel et al. (2013)
Diffusion coefficient (microbes)	D_m	2.1×10^{-9}	m ² /s	Kim (1996)
Diffusion coefficient (substrate)	D_s	5×10^{-10}	m ² /s	Hardy and Sarko (1993)
Diffusion coefficient (urea)	D_u	1.38×10^{-9}	m ² /s	Nanne et al. (2010)
Dispersion coefficient (longitudinal)	α_L	10^{-3}	m	Benekos et al. (2006)
Dispersion coefficient (transverse)	α_T	4×10^{-4}	m	Benekos et al. (2006)
Fitting factor	η	3	[-]	Hommel et al. (2013)
Half-velocity coefficient (substrate)	k_s	8×10^{-4}	kg/m ³	Taylor and Jaffé (1990)
Half-velocity coefficient (urea)	k_u	21.3	kg/m ³	Lauchnor et al. (2015)
Maximum rate of substrate utilization	μ_s	4.17×10^{-5}	1/s	Connolly et al. (2013)
Maximum rate of urea utilization	μ_u	1.61×10^{-2}	1/s	Lauchnor et al. (2015)
Microbial attachment rate	k_a	8.3753×10^{-8}	1/s	Hommel et al. (2015)
Microbial death rate	k_d	3.18×10^{-7}	1/s	Taylor and Jaffé (1990)
Minimum permeability	K_{min}	10^{-20}	m ²	Schlumberger (2020)
Water viscosity	μ_w	2.535×10^{-3}	Pa s	Ebigbo et al. (2007)
Yield coefficient (biomass/substrate)	Y_{sb}	0.5	[-]	Seto and Alexander (1985)
Yield coefficient (calcite/urea)	Y_{uc}	1.67	[-]	Universal

(2020) for the description of a novel sensitivity analysis method. Other common studies on these models are, for example, mathematical optimization and parameter uncertainty. In Tveit et al. (2020), we present an optimization study of a MICP model under parameter uncertainty.

2.5 Injection strategy

Diverse injection strategies have been studied for the MICP technology in laboratory experiments [e.g., Ebigbo et al. (2012), Kirkland et al. (2019), and Whiffin et al. (2007)] and numerical simulations [e.g., Hommel et al. (2015), Minto et al. (2019), and Tveit et al. (2018)]. In this work we consider the injection strategy shown in Fig. 3.

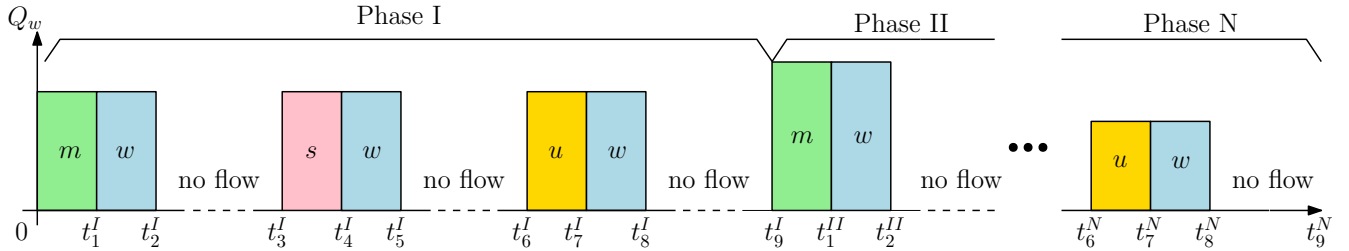


Figure 3: Injection strategy splitting into phases where m , s , u , and w refer to injection of microbes, substrate, urea, and only water respectively.

Given that the position of the well is fixed in the domain, the control variables for the injection strategy are the flux rate (water) along the height of the well, i.e., $Q_w(z, t)$ and concentrations of components (microbes, substrate, and urea). This injection strategy involves several phases where the three components are injected in the following order: microbes, substrate, and urea. First, microbes are injected for a total time t_1^I . This injection is followed by water injection (t_2^I) to move the microbes away from the injection well. Subsequently, there is a no-flow period to

facilitate attachment of microbes to the pore walls (t_3^I). Substrate is injected (t_4^I), followed by water displacement (t_5^I), and subsequently there is a no-flow period (t_6^I) to stimulate biofilm formation away from the injection well and around the sealing target. Urea is injected (t_7^I), displaced by water (t_8^I), and subsequently a no-flow period (t_9^I) to precipitate calcite at the sealing target. We refer to these nine stages as phase I. Several phases can be applied to decrease the permeability in the targeted zone, see Fig. 3.

3 Numerical studies

In this section, we consider several examples that are divided into two parts. In the first part we study MICP in systems where we target calcite precipitation at selected parts of the aquifer [e.g., [Minto et al. \(2019\)](#), [Nassar et al. \(2018\)](#), and [Tveit et al. \(2018\)](#)]. This mimics a situation where MICP technology is applied to prevent formation of leakage paths in the caprock, that is in regions with closed fractures/faults that could be opened when CO₂ is injected. In the second part we study MICP in systems where leakage paths are modeled explicitly [e.g., [Cunningham et al. \(2019\)](#)]. Here, we focus on the benchmark problem introduced in [Ebigbo et al. \(2007\)](#) and [Class et al. \(2009\)](#), where two aquifers are separated by a caprock with a leakage path.

For the numerical examples we consider two set of reservoir properties. The first set of properties is taken from [Tveit et al. \(2018\)](#), where the authors studied the MICP technology for sealing at a given distance of an injection well. One of the motivations to include the same properties in this work is to compare qualitatively the simulation results between the two different model implementations. The second set of properties is taken from [Ebigbo et al. \(2007\)](#). Let K_A denote the permeability in the aquifer, K_L the permeability of the leakage path, L the length, W the width, and H the height of the aquifer, h the height of the caprock, l the distance of the leakage zone from the well, a the aperture of the leakage path, and ω the aperture of the potential leakage zone. Table 2 summarizes the properties of both systems.

Table 2: Table of reservoir properties for the numerical studies

Reference	Example	ϕ	$K_A[\text{m}^2]$	$K_L[\text{m}^2]$	$L[\text{m}]$	$W[\text{m}]$	$H[\text{m}]$	$h[\text{m}]$	$l[\text{m}]$	$\omega[\text{m}]$	$a[\text{m}]$
Tveit et al. (2018)	1Dhd	0.2	10^{-12}	–	75	–	–	–	15	4	–
	2Dhcd	0.2	10^{-12}	–	75	–	–	–	15	4	–
	2Dhrd	0.2	10^{-12}	–	75	20	–	–	15	4	–
Ebigbo et al. (2007)	2Dvrd	0.15	2×10^{-14}	10^{-12}	500	–	30	–	100	20	–
	2Dld	0.15	2×10^{-14}	10^{-12}	500	–	30	100	100	–	0.3
	3Dld	0.15	2×10^{-14}	10^{-12}	500	1000	30	100	100	–	0.3

In the examples, we will perform simulations on 1D, 2D, and 3D domains. On each of the domains we will study different aspects of the injection strategy (Section 2.5) and the dynamics of the MICP process. The learnings from one domain will be useful by itself, but will also inform the studies on the other domains, ultimately leading up to running the 3D benchmark problem in the second part. Since this benchmark problem involves the solution on a large domain, we will neglect the dispersion effects to decrease the computational time (only for the 2Dld and 3Dld domains since we will compare their numerical results). We remark that for the numerical simulations the 1D and 2D domains are given as 3D grids (e.g., the 1D horizontal domain is represented by a grid of dimensions $L \times 1 \text{ m} \times 1 \text{ m}$).

3.1 MICP to prevent formation of leakage paths

Fig. 4 shows the four different domains we consider for the numerical experiments. In all experiments the potential leakage region is located at a distance l from the injection well. The simplest spatial domain for numerical studies is a 1D horizontal domain as shown in Fig. 4a. This domain consists of an injection well, a potential leakage region, and an open boundary. Two 2D horizontal extensions of this domain are given in Fig. 4b and Fig. 4c. The former represents a potential leakage region with a given aperture ω , while the latter represents a potential leakage region of aperture ω and width W . Fig. 4d shows a 2D vertical domain with a height H where the potential leakage region is on the top caprock.

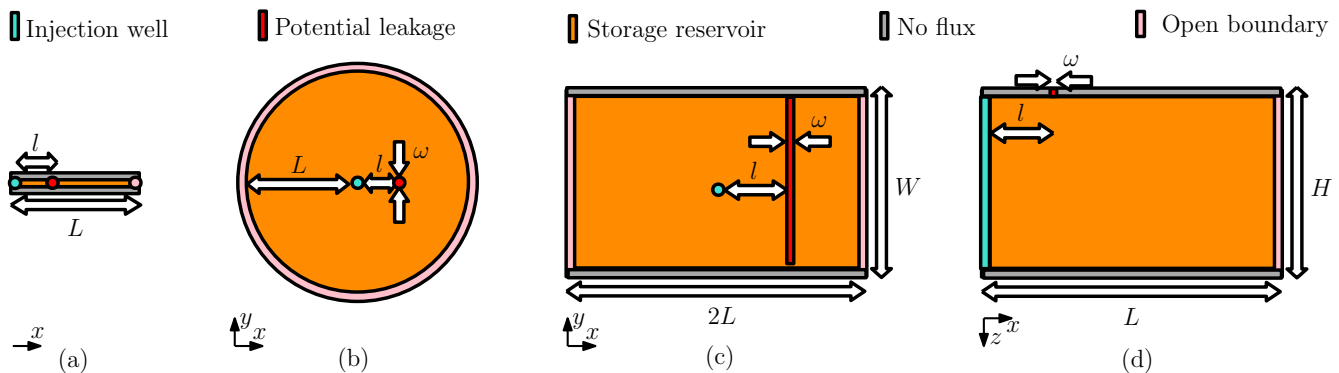


Figure 4: (a) 1D horizontal, (b) 2D horizontal circular, (c) 2D horizontal rectangular, and (d) 2D vertical domains.

3.1.1 1D horizontal domain (1Dhd)

We first investigate the dynamic evolution of the model components (i.e., microbes, substrate, urea, biofilm, and calcite) during the injection of phase I on the 1D horizontal domain in Fig. 4a. The different values for the times in the injection of phase I are the following: $t_1^I = 20$ h, $t_2^I = 40$ h, $t_3^I = 140$ h, $t_4^I = 160$ h, $t_5^I = 180$ h, $t_6^I = 230$ h, $t_7^I = 250$ h, $t_8^I = 270$ h, and $t_9^I = 300$ h. These injection times are identical to the ones studied in Tveit et al. (2018). Given the values of injection times, the corresponding injection rate which leads to permeability reduction on the target zone is $Q_w^I = 3.8 \times 10^{-5}$ m³/s. The numerical results are shown in Fig. 5. We observe that after 300 hours all urea is used to produce calcite around the potential leaky zone. The pore space around the target zone is reduced significantly after injection of phase I.

3.1.2 2D horizontal circular domain (2Dhcd)

We now consider the 2D horizontal circular domain in Fig. 4b studied in Tveit et al. (2018). The authors used a sequential approach to solve the mathematical model on a fine triangular grid, which was implemented using FiPY (Guyer et al., 2009). The main purpose of this example is to compare qualitatively with the results in Tveit et al. (2018). Most of the model parameters considered in Tveit et al. (2018) have the same values as in Table 1 or are of the same order of magnitude. The radius of the domain, target location of MICP, initial porosity, and permeability are the same as in the 1D experiment, which also are the mean values in the log-normal distributions in Tveit et al. (2018). We simulate the injection of one phase of MICP using the same injection times as in the previous example (1Dhd). We set the injection rate equal to the rate from the 1Dhd example multiplied by L , i.e., $Q_w^I = 2.8 \times 10^{-3}$ m³/s. Fig. 6 shows the grid, initial permeability, and permeability reduction for our numerical simulations. Here we remark that a scale factor is used to relate the flow rates between the domains. The corresponding scale factor

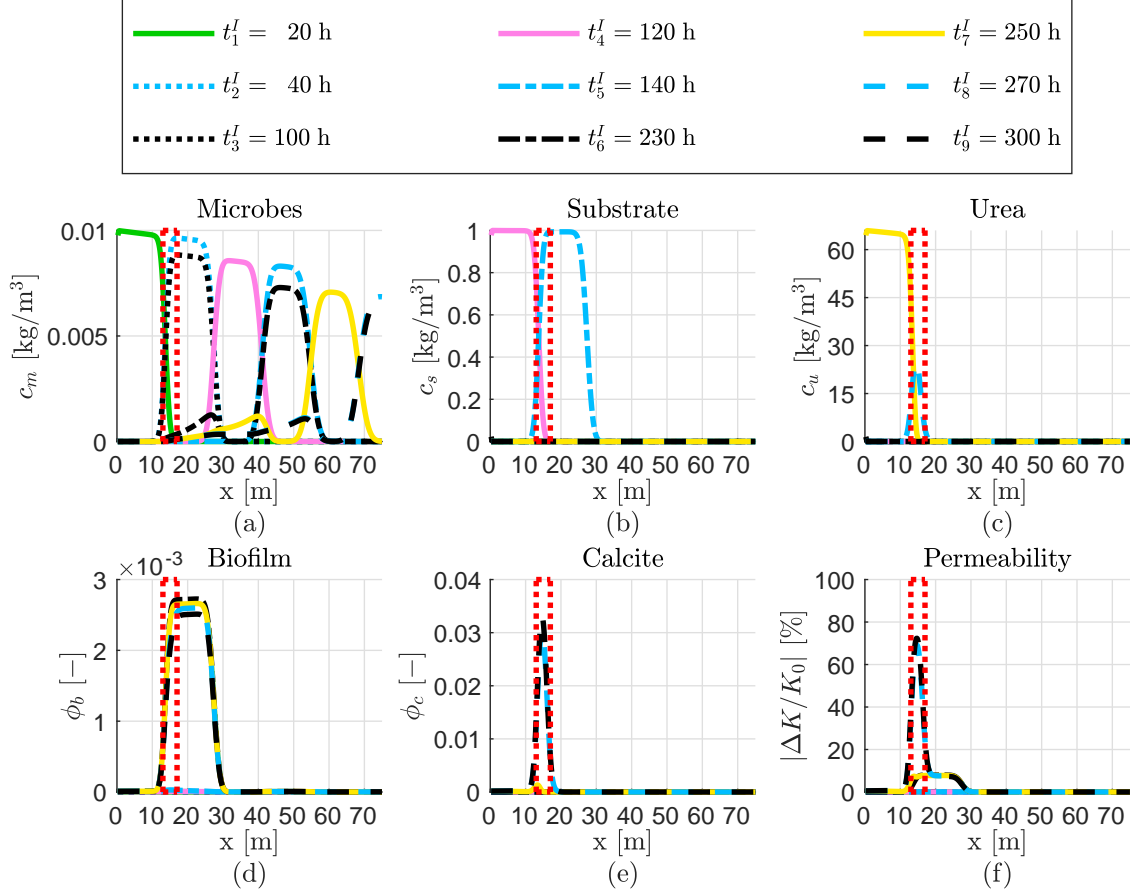


Figure 5: Spatial distribution of (a) microbes, (b) substrate, (c) urea, (d) biofilm, (e) calcite, and (f) permeability at different times in the injection strategy. The potential leakage region is inside the red rectangle.

from the 1Dhd to the 2Dhd is given by the radius L which results in reduction of permeability at the same distance from the injection well in both domains as shown in Figs. 5f and 6b.

Comparing qualitatively the permeability reduction reported in Tveit et al. (2018) to the one seen in Fig. 6b, we observe that both simulations predict the reduction of permeability at the targeted distance from the injection well of 15 m. The different approaches to model the biofilm detachment [e.g., detachment from growing biofilm in Tveit et al. (2018) and detachment due to erosion in this work] and the numerical schemes [sequential in Tveit et al. (2018) and fully implicit in this work] results in the discrepancies [i.e., difference in the value and diffuse rings outside the target area in Tveit et al. (2018)] between the predicted permeability reductions. In addition, the computational cost of the present grid is lower compared to the uniform fine triangular grid studied in Tveit et al. (2018). Thus, in the subsequent experiments, we discretize the spatial domain in a similar manner as shown in Fig. 6a, where the grid around the injection well and the region where the calcite precipitation occurs is fine (order of tens of centimeter), and gradually make it coarser (order of meters) towards the domain boundaries.

3.1.3 2D horizontal rectangular domain (2Dhrd)

We focus on the 2D horizontal domain in Fig. 4c. We set the simulation domain size to $2L = 150$ m and $W = 20$ m. For this example we investigate the reduction of permeability in a potential leakage zone along the width of the aquifer. We simulate the injection of one phase of MICP using the same injection times as in the previous example.

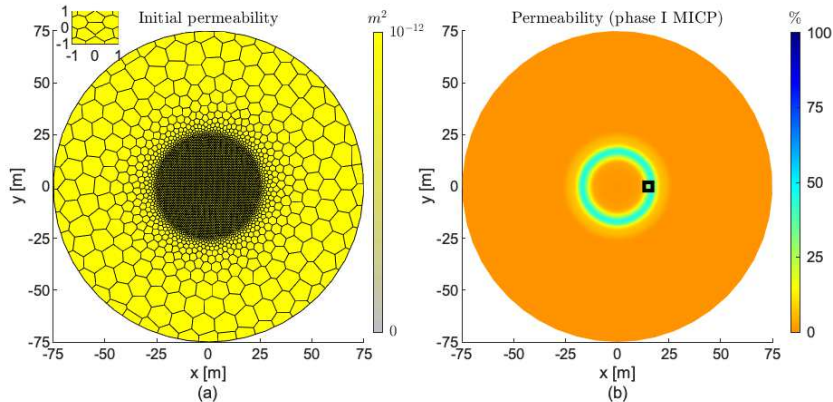


Figure 6: (a) Initial permeability and (b) permeability reduction after injection of phase I. The potential leakage region is inside the black square.

We set the injection rate equal to the rate from the 1Dhd example multiplied by W , i.e., $Q_w^I = 1.5 \times 10^{-3} \text{ m}^3/\text{s}$.

Fig. 7a shows the permeability reduction after phase I of the injection. We observe that the closer to the lateral boundaries we target the calcite precipitation, the further into the aquifer the components need to be injected, due to the radial flow. Consequently, not all parts of the potential leakage region are covered by one phase of MICP injection. We apply a second phase of injection with the same concentrations and time intervals as phase I but at a higher injection rate $Q_w^{II} = 2Q_w^I$. This higher injection rate for the second phase is selected after testing different injection rates. Fig. 7b shows the permeability reduction after a second phase of injection. Thus, several injection phases at different rates are needed to reduce the permeability inside the potential leakage region.

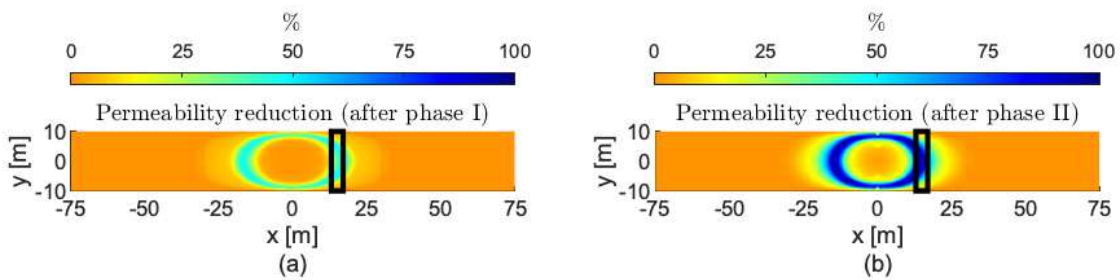


Figure 7: Permeability reduction after injection of (a) phase I and (b) phase II. The potential leakage region is inside the black rectangle.

3.1.4 2D vertical rectangular domain (2Dvrd)

In the next example we study the 2D vertical domain shown in Fig. 4d. We set the simulation domain size following the benchmark study in Ebigbo et al. (2007), that is, $L = 500 \text{ m}$ and $H = 30 \text{ m}$. We simulate the injection of one phase of MICP using the same injection times as in the previous example. We investigate two different injection

approaches along the well for the components and water to efficiently get calcite precipitation at the potential leakage region in the caprock. For the first simulation the injection of components and water is only in the first 3 m of the well. For the last simulation we change the water injection to be along the whole height of the well. Given that the distance to the leakage zone for this reservoir is larger than the one in the previous examples, then a larger injection rate is needed. An injection rate which leads to permeability reduction on the target zone is $Q_w^I = 6 \times 10^{-3} \text{ m}^3/\text{s}$.

Fig. 8 shows the permeability reduction for both injection approaches. We observe that the first injection approach leads to calcite precipitation also along the vertical direction. This is not desired as it could lead to encapsulation of the injection well. With the second injection approach, we accomplish calcite precipitation around the potential leakage region located near the caprock. Then we consider the latter injection approach in the next examples where vertical wells are also simulated.

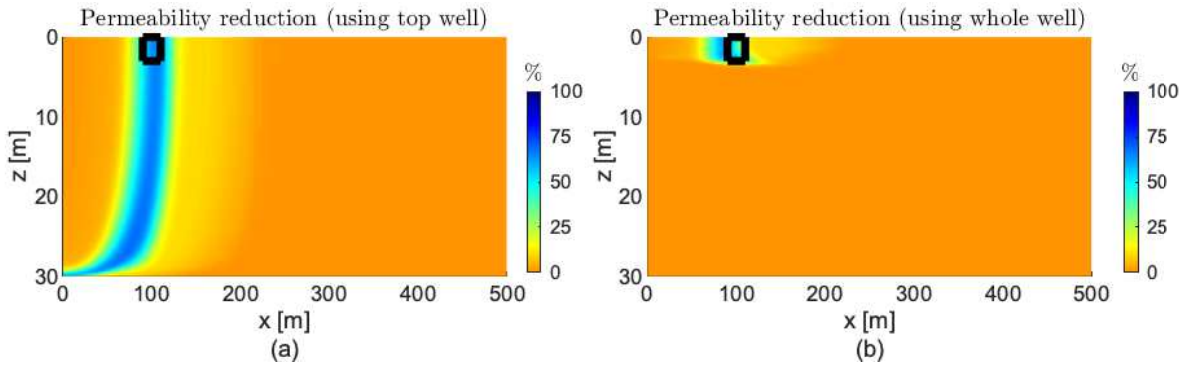


Figure 8: Permeability reduction (a) only using the top of the well and (b) the whole well. The potential leakage region is inside the black rectangle.

3.2 MICP to seal leakage paths

Diverse reservoir representations where leakage paths are explicitly modeled can be found in literature. In this work, we focus on the two domains shown in Fig. 9. A simple representation of a 2D domain with one leakage path between two aquifers is shown in Fig. 9a. A well-established 3D benchmark for CO_2 leakage is given by the domain in Fig. 9b (Class et al., 2009; Ebigbo et al., 2007).

3.2.1 2D leaky domain (2Dld)

We focus on the domain shown in Fig. 9a. In Ebigbo et al. (2007) the leakage is given as a result of a well which is modeled as a porous medium with higher permeability than the formation. To assess the leakage rate of CO_2 before and after application of MICP, we solve a simple two-phase flow model for CO_2 and water (see Appendix A).

We simulate the injection of one phase of MICP using the same injection times and injection rate as in the previous example (2Dvrd). After simulation the observed permeability reduction in the leakage path was minor. One alternative is to apply additional phases of MICP at different flow rates keeping the same time intervals to aim for the sealing of the leakage path. Since performing simulations on this 2D domain is computationally cheap, we proceed to design an injection strategy such that a minimum number of phases are needed for the sealing of the leakage path. It is beyond the scope of this paper to perform optimization studies. Here we use an ad-hoc approach where we keep the same order of injection of the components, values of concentrations, height of injection along the

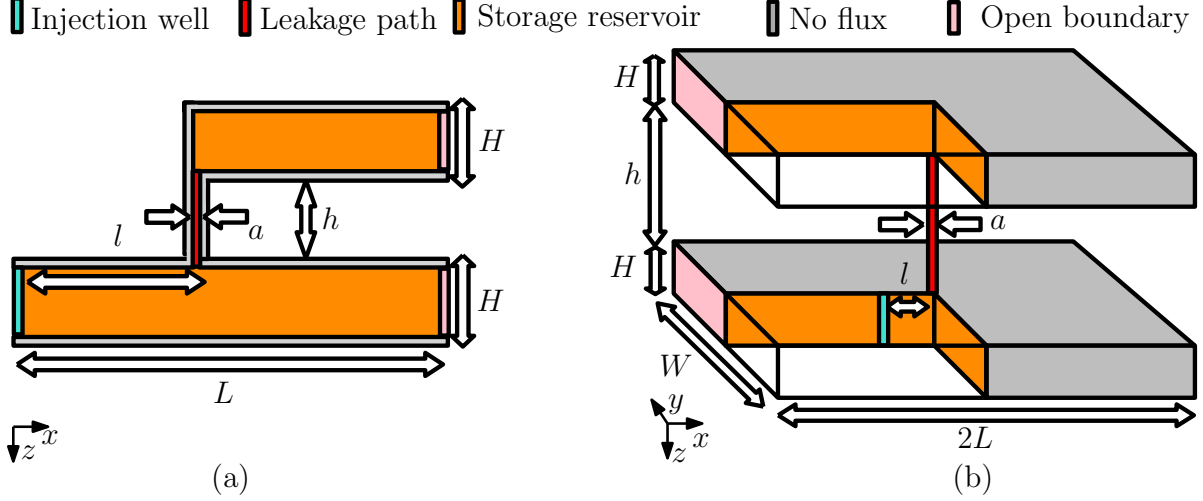


Figure 9: (a) 2D leaky domain and (b) 3D leaky well.

well, and total time of injection of one phase as in all previous examples. Using insight gain from previous studies, we perform several simulations where injection times and rates are changed manually. The following times and rates lead to the sealing of the leakage path after injection of two phases: $t_1^I = 20$ h, $t_2^I = 30$ h, $t_3^I = 100$ h, $t_4^I = 130$ h, $t_5^I = 140$ h, $t_6^I = 230$ h, $t_7^I = 270$ h, $t_8^I = 290$ h, $t_9^I = 300$ h, $Q_w^I = 8 \times 10^{-3}$ m³/s, $t_i^{II} = t_i^I + 300$ h ($i \in \{1, \dots, 9\}$), and $Q_w^{II} = 5Q_w^I$. Fig. 10 shows the numerical results of this injection strategy on the 2D leaky domain.

For a better visualization of the different MICP processes, in Fig. 11a we plot the average value normalized by its maximum value achieved in phase I or II for water velocity, microbial, substrate, and urea concentrations, biofilm and calcite volume fractions, and permeability reduction in the leakage path. We observe a remarkably increase of calcite after injection of urea in phase II which in turn decreases significantly the volume fraction of biofilm. Fig. 11b shows the leakage rate without and after MICP injection of phase I and II after 100 days of CO₂ injection. In the numerical results, we calculate the leakage as the CO₂ flux at the middle of the leaky well ($z = 80$ m) (Ebigbo et al., 2007). We observe that the leakage rate is practically stopped after two phases.

3.2.2 3D leaky domain (3Dld)

We consider the 3D benchmark reservoir as described in Class et al. (2009) and Ebigbo et al. (2007) shown in Fig. 9b. Since the properties of the previous domain (2Dld) are also equal to the ones in the benchmark, we expect to obtain similar results after applying the same injection strategy. Thus, we simulate the injection of two phases of MICP using identical time intervals as in the previous example. We set the injection rate equal to the rate from the 2Dld example multiplied by L , i.e., $Q_w^I = 4$ m³/s. Fig. 12 shows the numerical results after applying phase I and II of MICP.

Fig. 13 shows the different MICP processes at the leaky well and the leakage rate before and after MICP treatments. We observe that the dynamics of the processes are similar to the ones plotted for the 2D leaky domain. We also observe that the curve without MICP injection is in good agreement with the ones presented in the benchmark study for CO₂ leakage in Class et al. (2009). Then, as observed in the 2D leaky domain, the leakage stops after applying two phases of MICP treatment.

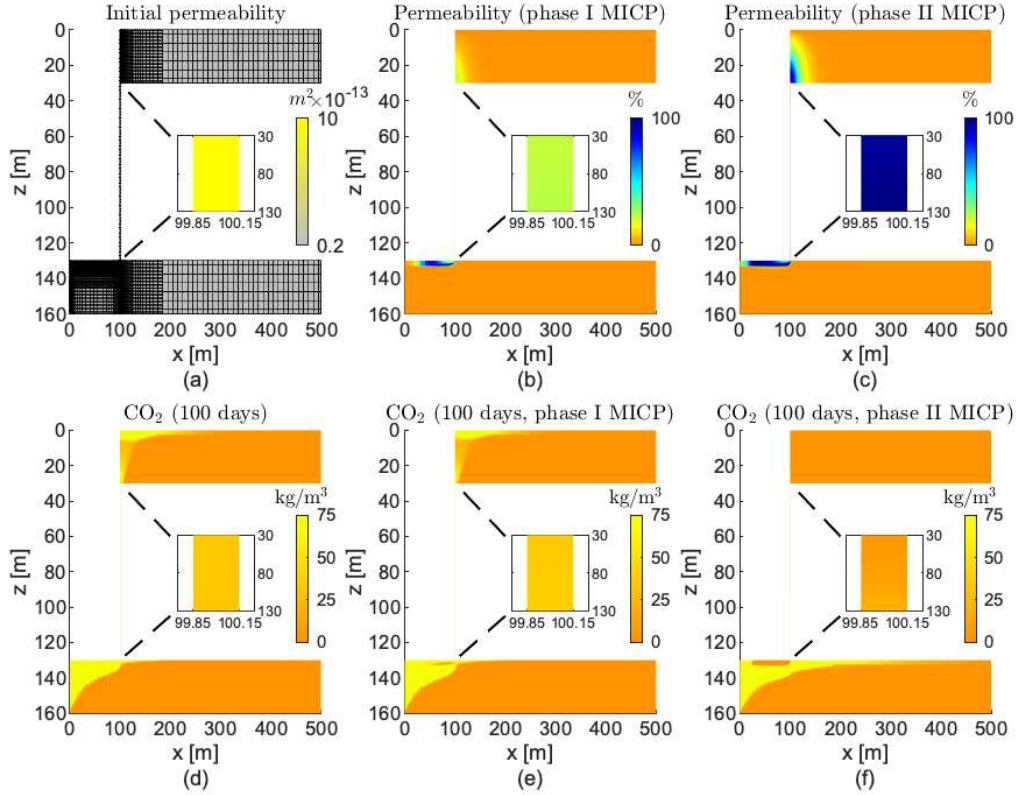


Figure 10: (a) Initial permeability, (b-c) permeability reductions after phase I and II, and (d-f) amount of CO_2 in the three different scenarios.

4 Discussion

The first part of the numerical examples includes MICP simulations to prevent the formation of leakage paths in an aquifer. We first study the spatial distribution of the diverse MICP variables (namely microbes, substrate, urea, biofilm, and calcite) on a simple 1D horizontal domain. Simulations on this domain are suitable for testing large numbers of injection strategies as it requires the lowest running time. In the 2D horizontal circular domain the potential leaky zone is given by a small area at a given distance from the injection well. However, the fluid injection through the well is in all horizontal directions leading to calcite precipitation around the injection well. To only target the potential leaky zone then the direction of injection could be controlled to decrease the cost of injected components and to not reduce the aquifer storage capability in unnecessary regions. Whereas this is an evident observation, we could not find experimental nor numerical studies involving directional wells in the literature. Thus, including directional wells in the simulators could be useful for MICP studies. An important observation of the simulations on the 2D horizontal rectangular domain is that several phases of injections might be needed to precipitate calcite along the width of the aquifer as a result of the radial flow from the well. The last example in the first part is a 2D vertical rectangular domain. Here we study the injection of water and components along the well. When we inject only at the top of the well, the calcite “encapsulates” the injection well along the vertical direction. We have observed that calcite precipitation only near the caprock is achieved injecting the components only at the top and water along the well. In the numerical studies we designate an arbitrary fixed part of the well for the injection of the components. However, the choice of this control variable is likely to have a significant

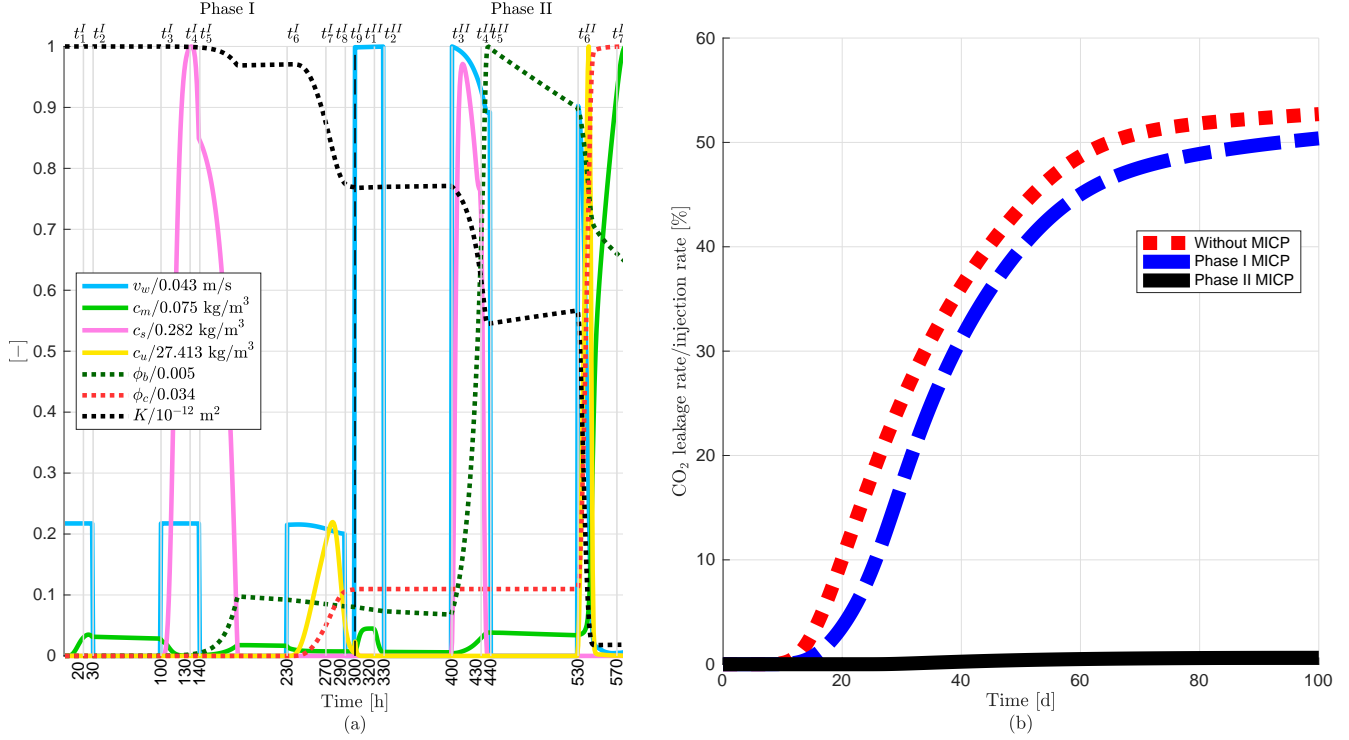


Figure 11: (a) Normalized variables and (b) leakage rate of CO₂ through the leaky region in the caprock.

impact in the simulations (e.g., due to transversal dispersion of the components). Hence, diverse injection heights should be studied for different systems to cut the injection times/cost.

The second part of the numerical examples focus on MICP simulations on domains where the leakage paths are modeled explicitly. We first study the sealing of a leakage path in a caprock between two aquifers on a simple 2D domain. We proceed to find values of time intervals and injection rates to achieve sealing in the leakage path. The designed injection strategy leads to sealing of the leakage path after two phases of MICP injection. The last numerical experiment is performed on a 3D benchmark leaky well. Since reservoir properties of both domains are equal, we use the same injection strategy as in the 2D domain. After simulations, we observe that the leakage path is blocked successfully. Despite the satisfactory and straightforward application of the injection strategy from the 2D domain to the 3D leaky well, this is ultimately restricted by the simplicity of the 3D domain. For instance, a different injection strategy should be designed for a 3D domain with a fracture across the width of the caprock. As observed in the simulations on the 2D horizontal rectangular domain in Fig. 7, we expect that several phases of MICP injection are required to significantly reduce the permeability in the leakage path.

The MICP model presented in this paper is built from a simplified description of the underlying processes based on previous publications as described in Section 2. The mathematical model is simple enough to have a few equations (six mass balance equations and six cross coupling constitutive relationships) and input parameters (twenty-one parameters) but still retain the essence of the processes. Extending the model to two-phase flow (water+MICP and CO₂) lets us consider additional processes, e.g., dissolution of calcite due to the presence of CO₂; however, solving simultaneously all equations would limit the size of the problem as discussed in Cunningham et al. (2019). As proposed by the authors, this could be solved by applying multi-physics methods, e.g., using analytical solutions for the flow.

Differences between the leakage rate curves on Figs. 11 and 13 arise from different issues. Prior to MICP

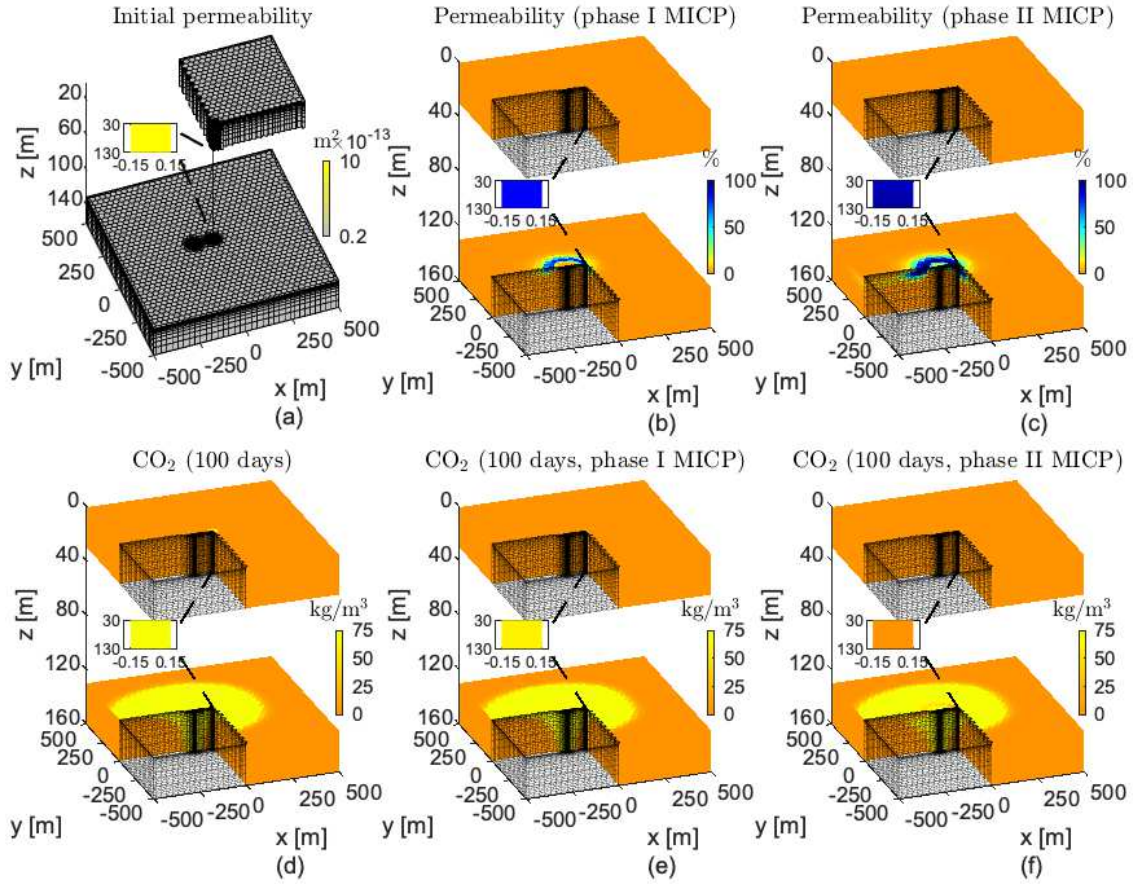


Figure 12: (a) Initial permeability, (b-c) permeability reductions after phase I and II, and (d-f) amount of CO₂ in the three different scenarios.

treatment, the percentage of leakage rate on the 2Dld is nearly 50% while for the 3Dld is lower than 0.25%. The reason for this difference is that on the 2D system all CO₂ injected either flows under or through the leakage path while for the 3D system only a small portion of CO₂ flows under and through the leakage path (since the flow is radial in the 3D system). Nevertheless, we would expect to have a similar curve shape for both systems. For the 3D system we observe a sharp rise of CO₂ leakage when the CO₂ reaches the leakage zone (approximately after 10 days of injection) and then drops (approximately after 50 days of injection). This is attributed to boundary effects (Ebigbo et al., 2007), as the CO₂ leakage is expected to continue increasing slowly after the initial sharp rise as shown in Fig. 11 (Nordbotten et al., 2005).

In addition, we observe a different decrease of CO₂ leakage after one phase of MICP treatment in both systems. From Fig. 11a we observe that the permeability reduction on the leakage path for the 2Dld system is around 25% while for the 3Dld system is around 80% (Fig. 13a). In this work we describe the 2Dld as a general simple system to study MICP in a leakage path. This domain is commonly related to an approximation of a system with a fault across the caprock [e.g., see Tavassoli et al. (2018)]. Thus, numerical simulations in both systems (2Dld and 3Dld domains) lead to different flux rates and velocities in the leakage path which in turn result in different permeability reduction after application of phase I (this explains the differences between velocities, concentrations, volume fractions, and permeability reduction values in Figs. 11a and 13a). For these examples we observe that

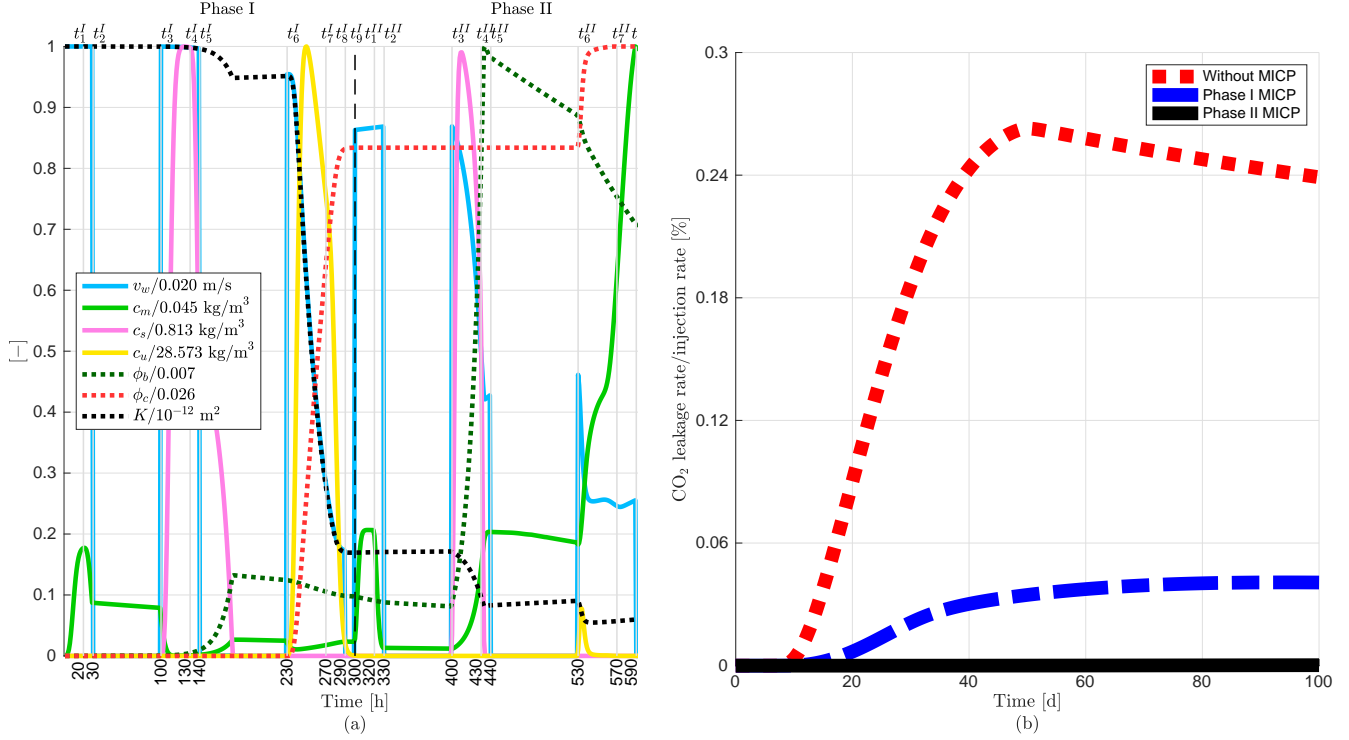


Figure 13: Leakage rate through the leaky region in the caprock.

the flow velocity through the leakage path is slower in the 2Dld domain than in the 3Dld. From the mathematical model (Eq. 8) we observe that the calcite precipitation is very sensitive to urea availability and biofilm formation. As a consequence of the difference between velocities, the whole MICP process is slow down in the 2Dld domain in comparison to the 3Dld domain. In addition, from Fig. 10 we observe calcite precipitation between the injection and leaky well while from Fig. 12 we observe calcite precipitation outside this region, i.e., between the injection well and outer boundary, since the flow field in the 3D domain also transport the different components around the leakage zone. Then the difference between both flow fields have an impact on the MICP processes in the leakage path as observe in Figs. 11a and 13a.

Notwithstanding these differences, the leakage path is successfully remediated in both systems (2Dld and 3Dld domains) after application of the second MICP treatment. A comprehensive investigation of boundary and grid effects, in addition to studies in more complex 3D domains, is not feasible using the current implementation of the mathematical model. Here we have used MRST for the testing of the model as implementation on this framework is not difficult; however, there are computation time limitations using this toolbox. Our current plan is to implement this mathematical model using the open porous media (OPM) initiative which allows to perform more computationally challenging simulations (Rasmussen et al., 2020). Hence we will use the OPM simulator to study these effects and MICP in more complex 3D domains.

In this work we only study one injection strategy for the MICP application consisting of several periodical phases. As described above, each phase involves the injection of three components, injection of only water, and periods of no flow, given a total of 18 control variables: three concentrations, six injection rates, and nine period times. To enable other researchers to benefit from our work and test different injection strategies, we have made the code available through a repository. Optimization could be applied to this problem, e.g., considering the costs of injected components, required energy for injection, and total time of injection. Moreover, changing the sequence

of components for the subsequent phases could lead to a better injection strategy, e.g., injection of substrate after the first phase for microbial resuscitation. Then, studying different sequence of components plus different heights of the well adds more complexity to the optimization. Though beyond the scope of the current work, further study in this direction is needed for optimization of the MICP technology.

5 Conclusions

In this work, we present a mathematical model for the MICP technology including the transport of injected components (microbes, substrate, and urea), biofilm formation, and calcite precipitation. We study an injection strategy involving several phases where each phase includes microbes, substrate, and urea with periods of only injection of water and no flow. We conduct diverse numerical experiments for various one- and two-dimensional domains to study the MICP process. Finally, we show the results of applying MICP to a well-established 3D benchmark problem for CO₂ leakage.

Based on this work conclusions are as follows:

- Learnings from 1D and 2D studies help us to develop practical injection approaches for 3D simulations.
- Only using a part of the well for injection of components and water leads to calcite precipitation along the whole vertical direction; however, using the top part of the well for injection of components and the rest of the well for water injection leads to calcite precipitation on the top of the aquifer.
- Several phases of injection might be needed for decreasing the permeability in (potential) leakage regions as a result of the radial flow by the injection well.
- Numerical simulations show a stop in CO₂ leakage after MICP treatment.

Appendix A Two-phase flow mathematical model for CO₂ and water

We describe the simplified two-phase flow model used in [Class et al. \(2009\)](#) for a benchmark study in problems related to CO₂ storage. CO₂ and water are assumed immiscible and incompressible. We denote by s_w the water saturation and s_{CO_2} the CO₂ saturation ($s_w + s_{CO_2} = 1$). We write Darcy’s law and the mass conservation equations for each α phase ($\alpha = w, CO_2$)

$$\mathbf{v}_\alpha = -\frac{k_{r,\alpha}}{\mu_\alpha} \mathbb{K}(\nabla p_\alpha - \rho_\alpha \mathbf{g}), \quad \phi \frac{\partial s_\alpha}{\partial t} + \nabla \cdot \mathbf{v}_\alpha = q_\alpha \quad (\text{A-1})$$

where $k_{r,\alpha}$ is relative permeability. The relative permeabilities are set as a linear function of the saturations ($k_{r,\alpha} = s_\alpha$), and capillary pressure is neglected ($p_w = p_{CO_2}$). The model parameters are summarized in [Table A-1](#).

Table A-1: Table of input variables and model parameters for the CO₂ leakage assessment.

Parameter	Symbol	Value	Unit
CO ₂ viscosity	μ_{CO_2}	3.95×10^{-5}	Pa s
CO ₂ density	ρ_{CO_2}	479	kg/m ³
Injected CO ₂	Q_{CO_2}	1.6×10^3	m ³ /day
Total time of injection	T_f	100	days

Notation

a	Aperture of the leakage path, [m]
c_m, c_s, c_u	Microbial, substrate, and urea concentrations, [kg/m ³]
$\mathbb{D}_m, \mathbb{D}_s, \mathbb{D}_u, D_m, D_s, D_u$	Microbial, substrate, and urea dispersion coefficients (tensor and scalar), [m ² /s]
\mathbf{g}	Gravity, [m/s ²]
H, h	Heights of the aquifer and caprock, [m]
$\mathbf{J}_m, \mathbf{J}_s, \mathbf{J}_u$	Microbial, substrate, and urea fluxes, [kg/(s m ²)]
\mathbb{K}, K	Rock permeability (tensor and scalar), [m ²]
K_A, K_L, K_{\min}	Aquifer, leakage, and minimum permeabilities, [m ²]
k_a, k_d	Microbial attachment and death rates, [1/s]
$k_{r,\text{CO}_2}, k_{r,w}$	Relative permeabilities of CO ₂ and water
k_s, k_u	Half-velocity coefficients (substrate and urea), [kg/m ³]
k_{str}	Detachment rate, [m/(s Pa)]
L, l	Size of the domain and distance from the well to the leakage region, [m]
p_{CO_2}, p_w	CO ₂ and water pressures, [Pa]
p_I	Pressure inside the wellbore, [Pa]
Q_{CO_2}, Q_w	Injection rates of CO ₂ and water, [m ³ /s]
q_{CO_2}, q_w	Source/sink terms of CO ₂ and water, [1/s]
R_m, R_s, R_u	Microbial, substrate, and urea rates, [kg/(s m ³)]
r_I	Radius of the well, [m]
s_{CO_2}, s_w	CO ₂ and water saturation
t_n^N	Injection time n of phase N, [s]
T_f	Total time of CO ₂ injection, [s]
$\mathbf{v}_{\text{CO}_2}, \mathbf{v}_w$	CO ₂ and water velocities, [m/s]
\mathbf{v}	Effective velocity of water, [m/s]
Y_{sb}, Y_{uc}	Yield coefficients (substrate to biomass and urea to calcite)
z_{bh}	Reference depth (perforation), [m]
α_L, α_T	Longitudinal and transverse dispersion coefficients, [m]
η	Fitting factor (permeability-porosity relationship)
μ_{CO_2}, μ_w	CO ₂ and water viscosities, [Pa s]
μ_s, μ_u	Maximum rate of substrate and urea utilization, [1/s]
ω	Aperture of the potential leakage zone, [m]
ϕ	Rock porosity
ϕ_b, ϕ_c	Volume fractions of biofilm and calcite
ϕ_{crit}	Critical porosity
$\rho_b, \rho_c, \rho_{\text{CO}_2}, \rho_u, \rho_w$	Biofilm, calcite, CO ₂ , urea, and water densities, [kg/m ³]

Acknowledgements: This work was supported by the Research Council of Norway [grant number 268390].

Data availability: The simulator MRST can be obtained at <https://www.sintef.no/projectweb/mrst/>. Link to complete codes for the numerical studies can be found in <https://github.com/daavid00/MICP.git>. The mesh generator DistMesh used for the spatial discretization in some of the numerical studies can be found in <http://persson.berkeley.edu/distmesh/>.

References

- Bai, Y., Guo, X.-J., Li, Y.-Z., Huang, T., 2017. Experimental and visual research on the microbial induced carbonate precipitation by *Pseudomonas aeruginosa*. *AMB Express*. **7**, 57. <https://doi.org/10.1186/s13568-017-0358-5>.
- Bao, K., Lie, K.-A., Møyner, O., Liu, M., 2017. Fully implicit simulation of polymer flooding with MRST. *Comput. Geosci.* **21** (5-6), 1219-1244. <https://doi.org/10.1007/s10596-017-9624-5>.
- Bear, J., 1972. Dynamics of fluids in porous media. New York, New York, USA: Elsevier Science.
- Benekos, I.D., Cirpka, O.A., Kitanidis, P.K., 2006. Experimental determination of transverse dispersivity in a helix and a cochlea. *Water Resour. Res.* **42** (7), W07406. <https://doi.org/10.1029/2005WR004712>.
- Bentham, M., Kirby, G., 2005. CO₂ storage in saline aquifers. *Oil Gas Sci. Technol.* **60** (3), 559-567. <https://doi.org/10.2516/ogst:2005038>.
- Berre, I. Doster, F. Keilegavlen, E., 2019. Flow in fractured porous media: A review of conceptual models and discretization approaches. *Transp. in Porous Med.* **130**, 215-236. <https://doi.org/10.1007/s11242-018-1171-6>.
- Bhaduri, S. Debnath, N., Mitra, S., Liu, Y., Kumar, A., 2016. Microbiologically induced calcite precipitation mediated by *Sporosarcina pasteurii*. *J. Vis. Exp.* **110**, e53253. <https://doi.org/10.3791/53253>.
- Class, H., Ebigbo, A., Helmig, R. et al., 2009. A benchmark study on problems related to CO₂ storage in geologic formations. *Comput. Geosci.* **13**, 409-434. <https://doi.org/10.1007/s10596-009-9146-x>.
- Connolly, J., Kaufman, M., Rothman, A., Gupta, R., Redden, G. Schuster, M., Colwell, F., Gerlach, R., 2013. Construction of two ureolytic model organisms for the study of microbially induced calcium carbonate precipitation. *J. Microbiol. Methods.* **94** (3), 290-299. <https://doi.org/10.1016/j.mimet.2013.06.028>.
- Cunningham, A.B., Class, H., Ebigbo, A., Gerlach, R., Phillips, A.J., Hommel, J., 2019. Field-scale modeling of microbially induced calcite precipitation. *Comput. Geosci.* **23**, 399-414. <https://doi.org/10.1007/s10596-018-9797-6>.
- De Muynck, W., De Belie, N., Verstraete, W., 2010. Microbial carbonate precipitation in construction materials: A review. *Ecol. Eng.* **36** (2), 118-136. <https://doi.org/10.1016/j.ecoleng.2009.02.006>.
- Ebigbo, A., Class, H., Helmig, R., 2007. CO₂ leakage through an abandoned well: problem-oriented benchmarks. *Comput. Geosci.* **11**, 103-115. <https://doi.org/10.1007/s10596-006-9033-7>.
- Ebigbo, A., Phillips, A., Gerlach, R., Helmig, R., Cunningham, A.B., Class, H., Spangler, L.H., 2012. Darcy-scale modeling of microbially induced carbonate mineral precipitation in sand columns. *Water Resour. Res.* **48** (7), W07519. <https://doi.org/10.1029/2011WR011714>.
- Gomez, M.G., Anderson, C.A., Graddy, C.M.R., DeJong, J.T., Nelson, D.C., Ginn, T. R., 2017. Large-scale comparison of bioaugmentation and biostimulation approaches for biocementation of sands. *J. Geotech. Geoenviron. Eng.* **143** (5), 04016124. [https://doi.org/10.1061/\(ASCE\)GT.1943-5606.0001640](https://doi.org/10.1061/(ASCE)GT.1943-5606.0001640).
- Guyer, J. E., Wheeler, D., Warren, J.A., 2009. FiPy: Partial Differential Equations with Python. *Comput. Sci. Eng.* **11** (3), 6-15. <https://doi.org/10.1109/MCSE.2009.52>.

- Fang, Y., Baojun, B., Dazhen, T., Shari, D.-N., Wronkiewicz, D., 2010. Characteristics of CO₂ sequestration in saline aquifers. *Pet. Sci.* **7**, 83–92. <https://doi.org/10.1007/s12182-010-0010-3>.
- Furre, A.-K., Eiken, O., Alnes, H., Vevatne, J.N., Kiær, A.F., 2017. 20 years of monitoring CO₂-injection at Sleipner. *Energy Procedia.* **114**, 3916–3926. <https://doi.org/10.1016/j.egypro.2017.03.1523>.
- Hammes, F., Verstraete, W., 2002. Key roles of pH and calcium metabolism in microbial carbonate precipitation. *Re. Environ. Sci. Bio. Technol.* **1**, 3–7. <https://doi.org/10.1023/A:1015135629155>.
- Hardy, B., Sarko, A., 1993. Molecular dynamics simulation of cellobiose in water. *J. Comput. Chem.* **14** (7), 848–857. <https://doi.org/10.1002/jcc.540140710>.
- Haszeldine, R.S., Flude, S., Johnson, G., Scott, V., 2018. Negative emissions technologies and carbon capture and storage to achieve the Paris Agreement commitments. *Phil. Trans. R. Soc. A.* **376**, 20160447. <https://doi.org/10.1098/rsta.2016.0447>.
- Hommel, J., Cunningham, A.B., Helmig, R., Ebigbo, A., Class, H., 2013. Numerical investigation of microbially induced calcite precipitation as a leakage mitigation technology. *Energy Procedia.* **40**, 392–397. <https://doi.org/10.1016/j.egypro.2013.08.045>.
- Hommel, J., Lauchnor, E., Phillips, A., Gerlach, R., Cunningham, A.B., Helmig, R., Ebigbo, A., Class, H., 2015. A revised model for microbially induced calcite precipitation: Improvements and new insights based on recent experiments. *Water Resour. Res.* **51**, 3695–3715. <https://doi.org/10.1002/2014WR016503>.
- Jalili, M., Ghasemi, M.R., Pifloush, A.R., 2018. Stiffness and strength of granular soils improved by biological treatment bacteria microbial cements. *Emerging Sci. J.* **2** (4), 219–227. <https://doi.org/10.28991/esj-2018-01146>.
- Jiang, N.-J., Soga, K., 2017. The applicability of microbially induced calcite precipitation (MICP) for internal erosion control in gravel-sand mixtures. *Géotechnique.* **67**, 42–55. <https://doi.org/10.1680/jgeot.15.P.182>.
- Jin, C., Liu, D., Shao, A., Zhao, X., Yang, L., Fan, F., Yu, K., Lin, R., Huang, J., Ding, C., 2018. Study on healing technique for weak interlayer and related mechanical properties based on microbially-induced calcium carbonate precipitation. *PLOS ONE.* **13** (19), e0203834. <https://doi.org/10.1371/journal.pone.0203834>.
- Kirkland, C.M., Norton, D., Firth, O., Eldring, J., Cunningham, A.B., Gerlach, R., Phillips, A.J., 2019. Visualizing MICP with X-ray μ -CT to enhance cement defect sealing. *Int. J. Greenhouse Gas Control.* **86**, 93–100. <https://doi.org/10.1016/j.ijggc.2019.04.019>.
- Kim, Y., 1996. Diffusivity of Bacteria. *Korean J. Chem. Eng.* **13**, 282–287. <https://doi.org/10.1007/BF02705951>.
- Kumar, K., List, F., Pop, I., Radu, F., 2020. Formal upscaling and numerical validation of fractured flow models for Richards equation. *J. Comput. Phys.* **407**, 109138. <https://doi.org/10.1016/j.jcp.2019.109138>.
- Landa-Marbán, D., Liu, N., Pop, I.S., Kumar, K., Pettersson, P., Bødtker, G., Skauge, T., Radu, F.A., 2019. A pore-scale model for permeable biofilm: Numerical simulations and laboratory experiments. *Transp. Porous Med.* **127** (3), 643–660. <https://doi.org/10.1007/s11242-018-1218-8>.

- Landa-Marbán, D., Bødtker, G., Kumar, K., Pop, I.S., Radu, F.A., 2020. An upscaled model for permeable biofilm in a thin channel and tube. *Transp. Porous Med.* **132**, 83–112. <https://doi.org/10.1007/s11242-020-01381-5>.
- Landa-Marbán, D., Bødtker, G., Kumar, K., Pop, I.S., Radu, F.A., 2020. Mathematical modeling, laboratory experiments, and sensitivity analysis of bioplug technology at Darcy scale. *SPE J.* <https://doi.org/10.2118/201247-PA>.
- Lauchnor, E.G., Topp, D.M., Parker, A.E., Gerlach, R., 2015. Whole cell kinetics of ureolysis by *Sporosarcina pasteurii*. *J. Appl. Microbiol.* **118** (6), 1321–1332. <https://doi.org/10.1111/jam.12804>.
- Lee, C., Lee, H., Kim, O.B., 2018. Biocement fabrication and design application for a sustainable urban area. *Sustainability.* **10** (11), 4079. <https://doi.org/10.3390/su10114079>.
- Li, D., Ren, S., Rui, H., 2019. CO₂ leakage behaviors in typical caprock-aquifer system during geological storage process. *ACS Omega.* **4**, 17874–17879. <https://doi.org/10.1021/acsomega.9b02738>.
- Lie, K.-A., 2019. An introduction to reservoir simulation using MATLAB/GNU Octave: User guide to the MATLAB reservoir simulation toolbox (MRST). Cambridge University Press. <https://doi.org/10.1017/9781108591416>.
- Linville, J.L., Rodriguez, M., Mielenz, J. R., Cox, C. D., 2013. Kinetic modeling of batch fermentation for *Populus* hydrolysate tolerant mutant and wild type strains of *Clostridium Thermocellum*. *Bioresour. Technol.* **147**, 605–613. <https://doi.org/10.1016/j.biortech.2013.08.086>.
- Martin, V., Jaffré, J., Roberts, J. E., 2005. Modeling fractures and barriers as interfaces for flow in porous media. *SIAM Journal on Scientific Computing.* **26** (5), 1667–1691. <https://doi.org/10.1137/S1064827503429363>.
- Minto, J. M., Lunn, R. J., El Mountassir, G., 2019. Development of a reactive transport model for field-scale simulation of microbially induced carbonate precipitation. *Water Resour. Res.* **55**, 7229–7245. <https://doi.org/10.1029/2019WR025153>.
- Mitchell, A.C., Phillips, A., Schultz, L., Parks, S., Spangler, L., Cunningham, A.B., Gerlach, R., 2013. Microbial CaCO₃ mineral formation and stability in an experimentally simulated high pressure saline aquifer with supercritical CO₂. *Int. J. Greenhouse Gas Control.* **15**, 86–96. <https://doi.org/10.1016/j.ijggc.2013.02.001>.
- Nanne, E.E., Aucoin, C.P., Leonard, E.F., 2010. Shear rate and hematocrit effects on the apparent diffusivity of urea in suspensions of bovine erythrocytes. *ASAIO journal (American Society for Artificial Internal Organs : 1992)*. **56** (3), 151–156. <https://doi.org/10.1097/MAT.0b013e3181d4ed0f>.
- Nassar, M.K., Gurung, D., Bastani, M., Ginn, T.R., Shafei, B., Gomez, M.G., Graddy, C. M. R., Nelson, D. C & De-Jong, J. T., 2018 Large-scale experiments in microbially induced calcite precipitation (MICP): Reactive transport model development and prediction. *Water Resour. Res.* **54**, 480–500. <https://doi.org/10.1002/2017WR021488>.
- Nordbotten, J., Celia, M., Bachu, S., Dhale, H.K., 2005. Semi-analytical solution for CO₂ leakage through an abandoned well. *Environ. Sci. Technol.* **39** (2), 602–611. <https://doi.org/10.1021/es035338i>.
- Norland, S., Heldal, M., Tmyr, O., 1987. On the relation between dry matter and volume of bacteria x-ray analysis. *Microbial Ecol.* **13**, 95–101. <https://doi.org/10.1007/BF02011246>.
- Peaceman, D.W., 1978. Interpretation of well-block pressures in numerical reservoir simulation. *Soc. Petrol. Eng. J.* **18** (3), 183–194. <https://doi.org/10.2118/6893-PA>.

- Persson, P.-O., Strang, G., 2004. A simple mesh generator in MATLAB. *SIAM Review*. **46** (2), 329–345. <https://doi.org/10.1137/S0036144503429121>.
- Phillips, K.S., Cunningham, A.B., Gerlach, R., Hiebert, R., Hwang, C., Lomans, B.P., Westrich, J., Mantilla, C., Kirksey, J., Esposito, R., Spangler, L., 2016. Fracture sealing with microbially-induced calcium carbonate precipitation: A field study. *Environ. Sci. Technol.* **50** (7), 4111–4117. <https://doi.org/10.1021/acs.est.5b05559>.
- Qin, C.-Z., Hassanizadeh, S.M., Ebigbo, A., 2016. Pore-scale network modeling of microbially induced calcium carbonate precipitation: Insight into scale dependence of biogeochemical reaction rates. *Water Resour. Res.* **52**, 8794–8810. <https://doi.org/10.1002/2016WR019128>.
- Rasmussen, A.F., Sandve, T.H., Bao, K., Lauser, A., et al., 2020. The Open Porous Media flow reservoir simulator. *Comput. Math. Appl.* <https://doi.org/10.1016/j.camwa.2020.05.014>.
- Rittmann, B.E., 1982. The effect of shear stress on biofilm loss rate. *Biotechnol. Bioeng.* **24** (2), 501–506. <https://doi.org/10.1002/bit.260240219>.
- Rong, H., Qian, C.-H., Li, L.Z., 2012. Study on microstructure and properties of sandstone cemented by microbe cement. *Constr. Build. Mater.* **36**, 687–694. <https://doi.org/10.1016/j.conbuildmat.2012.06.063>.
- Schlumberger, 2020. Cap rock. https://www.glossary.oilfield.slb.com/en/Terms/c/cap_rock.aspx (accessed 13 October 2020).
- Seto, M., Alexander, M., 1985. Effect of bacterial density and substrate concentration on yield coefficients. *Appl. Environ. Microbiol.* **50** (5), 1132–1136.
- Tavassoli, S., Xu, Y., Sepehrnoori, K. 2018. Modeling fault reactivation using embedded discrete fracture method. Paper presented at the SPE annual technical conference and exhibition, Dallas, Texas, USA, 24-26 September. SPE-191412-MS. <https://doi.org/10.2118/191412-MS>.
- Taylor, S.W., Jaffé, P.R., 1990. Substrate and biomass transport in a porous-medium. *Water Resour. Res.* **26** (9), 2181–2194. <https://doi.org/10.1029/WR026i009p02181>.
- Thullner, M., Zeyer, J., Kinzelbach, W., 2002. Influence of microbial growth on hydraulic properties of pore networks. *Transp. Porous Med.* **49**, 99–122. <https://doi.org/10.1023/A:1016030112089>.
- Tong, D., Zhang, Q., Caldeira, K., Shearer, C., Hong, C., Qin, Y., Davis, S. J., 2019. Committed emissions from existing energy infrastructure jeopardize 1.5 °C climate target. *Nature*. **572**, 373–377. <https://doi.org/10.1038/s41586-019-1364-3>.
- Torres-Aravena, A. E., Duarte-Nass, C., Azócar, L., Mella-Herrera, R., Rivas, M., Jeison, D., 2018. Can microbially induced calcite precipitation (MICP) through a ureolytic pathway be successfully applied for removing heavy metals from wastewaters? *Crystals*. **8** (11), 438. <https://doi.org/10.3390/cryst8110438>.
- Tveit, S., Gasda, S.E., Hægland, H., Bødtker, G., Elenius, M., 2018. Numerical study of microbially induced calcite precipitation as a leakage mitigation solution for CO₂ storage. *European Association of Geoscientists & Engineers*. **2018**. <https://doi.org/10.3997/2214-4609.201802956>.
- Tveit, S., Pettersson, P., Landa-Marbán, D., 2020. Optimizing sealing of CO₂ leakage paths with microbially induced calcite precipitation under uncertainty. *European Association of Geoscientists & Engineers*. **2020**. <https://doi.org/10.3997/2214-4609.202035087>.

- van Noorden, T.L., Pop, I.S., Ebigbo, A., Helmig, R., 2010. An upscaled model for biofilm growth in a thin strip. *Water Resour. Res.* **46** (6), W06505. <https://doi.org/10.1029/2009WR008217>.
- Whiffin, V.S., van Paassen, L.A., Harkes, M.P., 2007. Microbial carbonate precipitation as a soil improvement technique. *Geomicrobiol. J.* **24** (5), 417–423. <https://doi.org/10.1080/01490450701436505>.
- Zhang, T., Klapper, I., 2010. Mathematical model of biofilm induced calcite precipitation. *Water Sci. Technol.* **61** (11), 2957–2964. <https://doi.org/10.2166/wst.2010.064>.